

Magnetization Plateaus in the Two-dimensional $S = 1/2$ Heisenberg Model with a 3×3 Checkerboard Structure

Xuyang Liang and Dao-Xin Yao*

Guangdong Provincial Key Laboratory of Magnetolectric Physics and Devices,
State Key Laboratory of Optoelectronic Materials and Technologies,
Center for Neutron Science and Technology, School of Physics,
Sun Yat-Sen University, Guangzhou, 510275, China

(Dated: August 23, 2024)

We investigate the $S=1/2$ antiferromagnetic Heisenberg model with a 3×3 checkerboard lattice structure in a longitudinal magnetic field. By using the stochastic series expansion quantum Monte Carlo (SSE-QMC) method, we obtain the properties of the non-plateau XY phase, $1/9$, $3/9$, $5/9$, $7/9$ magnetization plateau phases, and fully polarized phase. Then, we determine the precise phase transition critical points belonging to the 3D XY universality class through finite-size scaling. Moreover, we study the longitudinal and transverse dynamic spin structure factors of this model in different phases. For the non-plateau XY phase, the energy spectra present a gap between the low-energy gapless branch and the high-energy part under the competition of magnetic field and interaction. The gapless branch can be described by the spin wave theory in the canted antiferromagnetic phase of the effective “block spin” model. In the magnetization plateau phase, we identify that the excitation arises from localized disturbances within the sublattice, which are capable of spreading in momentum space. This study offers theoretical insights and interpretations for the characteristics of the ground state and the inelastic neutron scattering spectrum in two-dimensional quantum magnetic materials. Specifically, it focuses on materials with a checkerboard unit cell structure and odd-spin configurations under the influence of a longitudinal magnetic field.

I. INTRODUCTION

The $S = 1/2$ Heisenberg antiferromagnetic model has consistently garnered attention in the realms of condensed matter physics, due to its crucial significance in the investigation of cuprate superconductors [1–4], and quantum magnetic materials [5, 6]. Among that, the magnetization plateau is a quantum phenomenon of the antiferromagnetic Heisenberg model, which has been extensively reported in both theory and experiments. In the one-dimensional Haldane chain [7, 8], the zero magnetization plateau appears until a finite magnetic field closes the gap between the singlet of the ground state and the triplet state of the first excited state. Notably, all plateaus conform to the Oshikawa Yamanaka-Affleck (OYA) criterion ($n(s - m) = \text{integer}$) in one-dimensional spin system [9], where n represents the number of sites in each unit cell, s is the magnitude of spin and m is the magnetization per spin. Moreover, the magnetization plateau induced by quantum fluctuations has become a very active research field in geometric frustration systems [10–19].

Besides the properties of the ground state, we are interested in the dynamic properties of magnetic systems. In recent years, inelastic neutron scattering (INS) experiments have revealed many novel dynamic properties. The high-energy continuum appears near $(\pi, 0)$ in the INS experiments of La_2CuO_4 and $\text{Cu}(\text{DCOO})_2 \cdot 4\text{D}_2\text{O}$, which cannot be described by the linear spin wave of square lattice [20, 21]. Furthermore, the magnetic field induced

spontaneous magnon decays are observed in the compound $\text{Ba}_2\text{MnGe}_2\text{O}_7$ [22]. On the other hand, the numerical simulations also provide valuable results on exploring the dynamical properties. For example, the method of combining stochastic analytic continuation (SAC) with QMC can effectively reveal the dynamic properties of spin liquids and fractionalization at a deconfined quantum critical point [23, 24].

In two-dimensional (2D) systems, certain materials show checkerboard structures as evidenced by experimental studies, such as $\text{Bi}_2\text{Sr}_2\text{CaCu}_2\text{O}_{8+\delta}$ and $\text{Ca}_{2-x}\text{Na}_x\text{CuO}_2\text{Cl}_2$ [25, 26]. In previous work, the magnetic excitation mechanism of the checkerboard model has been investigated [27, 28]. Notably, the 3×3 checkerboard model shows the excitation of spin wave originating from inter-sublattice, due to each 3×3 plaquette having the odd number of spins. Furthermore, the one-dimensional trimer chains are a simplification of this model. It is found that the two-spinon continuum is described by the novel intermediate-energy and high-energy localized excitations are termed as the “doublon” and “quarton” for weak inter-trimer interaction J_2 , respectively. [29]. These excitations have been confirmed to exist in the experimental material $\text{Na}_2\text{Cu}_3\text{Ge}_4\text{O}_{12}$ [30]. Furthermore, such excitations are observed in the 2D theoretical model proposed based on $\text{Ba}_4\text{Ir}_3\text{O}_{10}$ and $\text{CaNi}_3(\text{P}_2\text{O}_7)_2$ with trimerized structure [31–36].

Recently, the one-dimensional trimer chains emerges the XY phase and $1/3$ magnetization plateau phase under the competition between the magnetic field and interaction, and propagates the “doublon” and “quarton” in a longitudinal magnetic field. [37]. For the 2D system, the 3×3 checkerboard model may induce more magne-

* yaodaox@mail.sysu.edu.cn

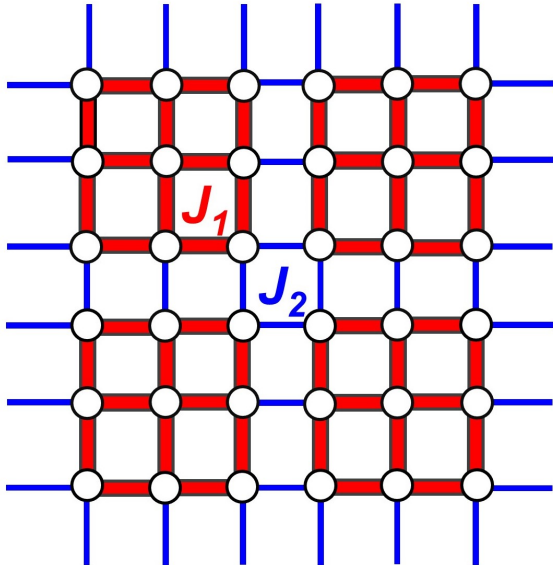


FIG. 1. Structure of 3×3 checkerboard lattice. The intra-sublattice interaction J_1 and the inter-sublattice interaction J_2 are represented by thick red and thin blue bonds, respectively.

tization plateaus and different fractional spin excitations in a magnetic field. In this paper, we investigate the properties of the ground state and spin dynamic of the $S = 1/2$ Heisenberg model on a 3×3 checkerboard lattice in a longitudinal magnetic field by using the SSE-QMC and SAC.

The rest of the paper is organized as follows. In Sec. II, we introduce the Hamiltonian of this model and the QMC-SAC method. In Sec. III, we study the critical points of phase transition based on the theory of finite-size scaling and present the results of the dynamic structural factors of the 3×3 checkerboard model in different magnetic fields. In Sec. IV, we explain the magnetic excitation mechanism of the magnetization plateau based on perturbation theory and discuss the excitation of the high-energy mode. The Sec. V is the summary of this article.

II. MODEL, METHOD, AND DEFINITIONS

A. Model

The Hamiltonian of the $S = 1/2$ antiferromagnetic Heisenberg model on a 3×3 checkerboard lattice in a longitudinal magnetic field can be written as

$$H = J_1 \sum_{\langle i,j \rangle} S_i \cdot S_j + J_2 \sum_{\langle i,j \rangle'} S_i \cdot S_j - h \sum_i S_i^z, \quad (1)$$

where S_i denotes the spin-1/2 operator on each site i ; $\langle i, j \rangle$ and $\langle i, j \rangle'$ represent the nearest-neighbor sites. The strong coupling J_1 and weak coupling J_2 correspond to the thick red and the thin blue bonds respectively, which represent antiferromagnetic nearest-neighbor interactions, and the longitudinal magnetic field is denoted by h in Fig. 1. We refer to each 3×3 plaquette as a sub-lattice and define the coupling ratio as $g = J_2/J_1$ in this paper. The value of J_1 is fixed to 1 as the energy unit, where the value of J_2 corresponds to g . We are interested in the whole range of coupling ratios g from 0 to 1, where the system evolves between the isolated sublattices ($g=0$) to antiferromagnetic Heisenberg square lattice with uniform interactions ($g=1$).

B. Quantum Monte Carlo method

We use the SSE-QMC simulation method to study the phase diagram and spectral functions of the 3×3 checkerboard model in this work [38]. Via SSE-QMC, we can obtain imaginary-time correlation functions. Due to the influence of the magnetic field, the symmetry of $SU(2)$ is broken. To comprehensively reveal the dynamic properties, the longitudinal and transverse imaginary-time correlation functions are measured, which are defined as

$$G_q^{zz}(\tau) = \frac{1}{N} \sum_{i,j} e^{-iq(r_i - r_j)} (\langle S_i^z(\tau) S_j^z(0) \rangle - \langle S_i^z(\tau) \rangle \langle S_j^z(0) \rangle), \quad (2)$$

$$G_q^\pm(\tau) = \frac{1}{4N} \sum_{i,j} e^{-iq(r_i - r_j)} (\langle S_i^+(\tau) S_j^-(0) + S_i^-(\tau) S_j^+(0) \rangle), \quad (3)$$

where r_i is the spatial position of the site i , the dynamic spin structure factor can be obtained by

$$G_q(\tau) = \int_{-\infty}^{\infty} d\omega \mathcal{S}(q, \omega) e^{-\tau\omega}. \quad (4)$$

In the SAC, the spectral function $\mathcal{S}(q, \omega)$ is parameterized by a large number of δ functions, and then the imaginary-time correlation functions $G_q(\tau)$ will be fitted through Monte Carlo simulation [39, 40].

III. NUMERICAL RESULTS

Here, we mainly study the 3×3 checkerboard lattice model with periodic boundary conditions under the influence of a longitudinal magnetic field.

A. Quantum phase transitions

To explore ground-state properties, we set up the inverse temperature $\beta = 4L$ in QMC simulation unless otherwise specified. First, we study the phase diagram of

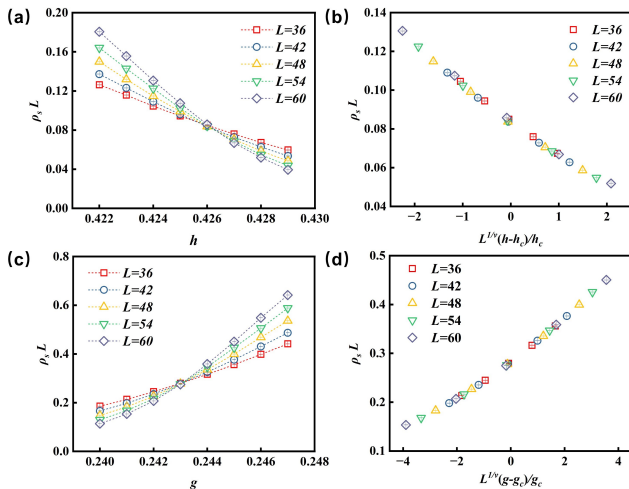


FIG. 2. (a) Spin stiffness multiplied by L at fixed $g=0.2$ versus the magnetic field h , and (c) spin stiffness multiplied by L at fixed $h=0.575$ versus the coupling ratio g . Panels (b) and (d) show the data collapses of spin stiffness multiplied by L , where the best fitting critical exponents ν are $0.667(5)$ and $0.669(2)$, respectively.

the $S = 1/2$ Heisenberg model on the 3×3 checkerboard square lattice in a longitudinal magnetic field. To investigate quantum phase transitions through QMC simulations, we employ spin stiffness ρ_s to probe the quantum critical points. Spin stiffness ρ_s is defined by the free energy f and the twist angle ϕ ,

$$\rho_s = \frac{1}{N} \frac{\partial^2 f}{\partial \phi^2}, \quad (5)$$

in the SSE simulations, the α (x or y) direction of spin stiffness can be calculated from

$$\rho_s^\alpha = \frac{1}{\beta N} \langle (N_\alpha^+ - N_\alpha^-)^2 \rangle, \quad (6)$$

where N_α^+ and N_α^- are actually the total number of the nearest off-diagonal operators $S_i^+ S_j^-$ and $S_i^- S_j^+$ transporting spin along the positive and negative α direction, respectively. In fact, we only calculate $\rho_s = \frac{(\rho_x + \rho_y)}{2}$ because the 3×3 checkerboard square lattice has isotropy. Meanwhile, at a quantum critical point, it should scale as

$$\rho_s \sim L^{2-d-z}, \quad (7)$$

where d is the dimension of the system, and z is the dynamic critical exponent. In our model, we have $d = 2$ and $z = 1$, and the scaling becomes $\rho_s \sim L^{-1}$. Thus, the $\rho_s L$ is size-independent at the critical point.

To obtain the quantum critical point, we determine the critical points h_c or g_c as shown in Fig 2(a) and (c), the clear crossing points indicate that a quantum phase

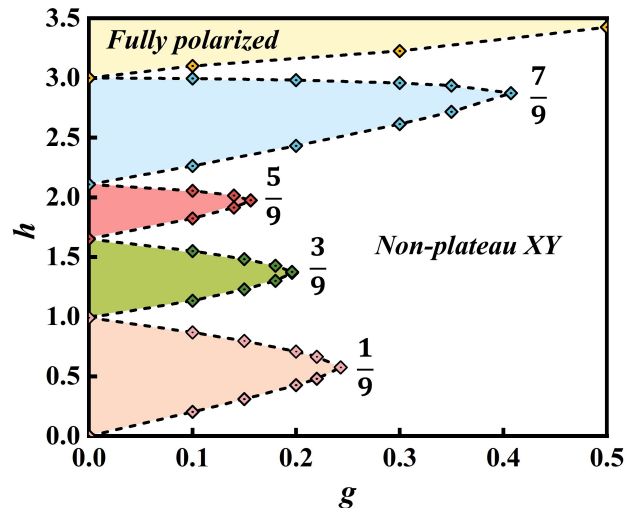


FIG. 3. The phase diagram of the $S = 1/2$ antiferromagnetic Heisenberg model on the 3×3 checkerboard lattice in a longitudinal magnetic field.

transition occurs between the non-plateau XY phase and the $1/9$ magnetization plateau phase.

On the basis of the theory of finite-size scaling, the spin stiffness scales as [41]

$$\rho_s(t, L) L = f(tL^{\frac{1}{\nu}}), \quad (8)$$

where ν is the correlation length exponent and $t = (\alpha - \alpha_c)/\alpha_c$, and the α_c represents h_c or g_c . We can obtain the α_c and ν from a data collapse, where the values of ν are $0.667(5)$ and $0.669(2)$ as shown in Figs. 2(b) and (d), respectively, indicating that the phase transition may belong to 3D XY universal class [42].

By using this method to calculate other values, we ultimately obtain the phase boundaries in Fig. 3. From this phase diagram, we can observe six different phases: $1/9$, $3/9$, $5/9$, and $7/9$ magnetization plateau phases, fully polarized phase, and non-plateau XY phase. To study the transverse long-range magnetic order of different phases, we define the square transverse staggered magnetization as

$$(m_\perp^s)^2 = \frac{1}{4N^2} \left(\sum_{ij} (-1)^{i+j} \langle S_i^+ S_j^- + S_i^- S_j^+ \rangle \right), \quad (9)$$

where $(-1)^{i+j} = \pm 1$ represents staggered phase factors. In Fig. 4, we show the transverse square staggered magnetization versus the magnetic field h in $g=0.1$. In the magnetization plateau phase, the size extrapolation shows that the transverse square staggered magnetization $(m_\perp^s)^2$ is zero in the thermodynamic limit as shown in the inset of Fig. 4.

In Fig. 5(b), the magnetization curve shows the magnetization process, where the magnetization per spin is

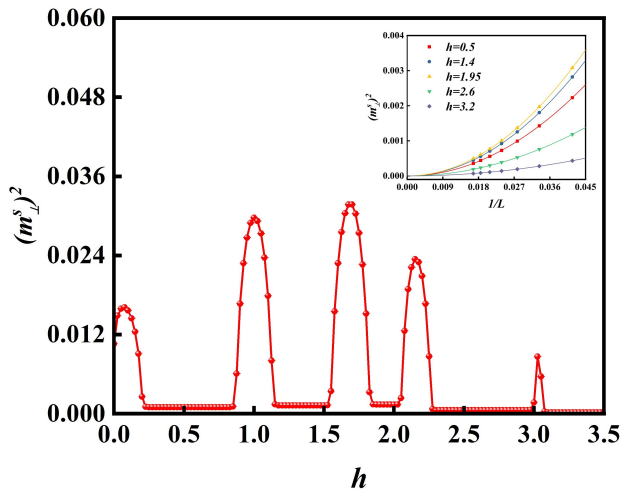


FIG. 4. The transverse staggered magnetization $(m_{\perp}^s)^2$ for $g=0.1$. The inset shows the results of finite size extrapolation in different magnetization plateau phases.

defined as $M_z = \sum_{i=1}^N S_i^z/N$, and M_z^s is the saturation magnetization per spin. We find that there are $1/9$, $3/9$, $5/9$, and $7/9$ magnetization plateaus when g is small. Meanwhile, the width of the plateaus decreases as g increases. Ultimately, all the magnetization plateaus vanish.

In addition, the magnetization of each spin and the nearest-neighbor spin correlation are calculated. The equivalent spins and spin correlations are represented by the same color in Fig. 5(a), we observe that it cannot form a $1/9$ magnetization plateau phase due to the magnetic field is not strong enough to open an energy gap at small h as shown in Fig. 5(b). As the magnetic field increases, antiferromagnetic correlations can be slowly suppressed, leading to the formation of a $1/9$ magnetization plateau phase. The four inequivalent spin correlations are as shown in Fig. 5(d), where the spin correlations $\langle S_i^z S_j^z \rangle_3$ and $\langle S_i^z S_j^z \rangle_4$ are ferromagnetic correlations, and the $\langle S_i^z S_j^z \rangle_1$ and $\langle S_i^z S_j^z \rangle_2$ are antiferromagnetic correlations in the $1/9$ magnetization plateau. Moreover, It is worth noting that the magnetizations of spin and spin correlations are fixed in the magnetization plateau as shown in Figs. 5(c) and 5(d). In the $1/9$ magnetization plateau phase, the magnetizations of three spins a, b, and c are $0.20095(3)$, $-0.11243(4)$, $0.14593(6)$, reflecting that each 3×3 sublattice can be regarded as an effective polarized spin $1/2$. Furthermore, other details of inequivalent spin magnetizations in the corresponding magnetization plateau phase are shown in Table I, where each 3×3 sublattice can be regarded as an effectively polarized spin $3/2$, $5/2$, and $7/2$ in the $3/9$, $5/9$ and $7/9$ magnetization plateau phases, respectively. Moreover, as the magnetic field increases, the spins a and b are further polarized until they are fully aligned. However, the nonmonotonic h -dependence behavior of the magnetization of spin c is observed in the regions $1.55 < h \leq 1.82$ and $2.05 < h \leq 2.26$,

TABLE I. The magnetization of each inequivalent spin in different magnetization plateau phases.

Magnetization plateau	a	b	c
$1/9(h=0.5)$	0.20095(3)	-0.11243(4)	0.14593(6)
$3/9(h=1.35)$	0.26341(3)	0.07287(4)	0.15489(7)
$5/9(h=1.95)$	0.35959(2)	0.23077(3)	0.13853(7)
$7/9(h=2.6)$	0.46954(1)	0.38688(1)	0.07429(5)

while the antiferromagnetic $\langle S_i^z S_j^z \rangle_2$ is stronger than others. Due to the magnetic field failing to suppress the strong coupling J_1 to completely polarize the spin c.

B. Excitation spectra

In this section, we study the longitudinal and transverse dynamical structure factors $S^{zz}(q, \omega)$ and $S^{\pm}(q, \omega)$ of the 3×3 checkerboard model in a longitudinal magnetic field by taking $g=0.7$, 0.4 and 0.1 . The lattice size L is chosen as 48 and 36 to calculate $S^{zz}(q, \omega)$ and $S^{\pm}(q, \omega)$ respectively when $g=0.7$ and 0.4 , and 48 for both $S^{zz}(q, \omega)$ and $S^{\pm}(q, \omega)$ when $g=0.1$. Inverse temperature is chosen to $\beta = L$ in QMC calculation. The results of $S^{zz}(q, \omega)$ and $S^{\pm}(q, \omega)$ are displayed along the high symmetry path $(0, 0) \rightarrow (\pi, 0) \rightarrow (\pi, \pi) \rightarrow (0, 0) \rightarrow (0, \pi) \rightarrow (\pi, 0)$ in the Brillouin zone. Among that, the convergence of the gapless point (π, π) with the spectral weight concentrated requires a very large β [39]. Consequently, we do not show it in the transverse excitation spectrum.

Firstly, we investigate the results of the 3×3 checkerboard model $S^{zz}(q, \omega)$ in a longitudinal magnetic field. In previous work, the 3×3 checkerboard lattice remains in the antiferromagnetic Néel phase, which exists gapless Goldstone mode at $(0, 0)$ and (π, π) [28]. The system enters from the antiferromagnetic Néel phase to the non-plateau XY phase driven by the magnetic field. When $g=0.7$, we find that the structures of the spectra are similar to the square lattice in a magnetic field [43], there is a gap proportional to the magnetic field at (π, π) and the spontaneous breaking of the $U(1)$ symmetry leads to the presence of a gapless Goldstone mode at $(0, 0)$. As the magnetic field increases, the gap at (π, π) increases, and the strong magnetic field leads to the spontaneous decay of magnons. Especially, the spectrum weight tends to vanish except for the vicinity of $(0, 0)$ in the strong magnetic field as shown in Fig. 6(d). For the spectra of $S^{\pm}(q, \omega)$, the Goldstone theorem indicates that antiferromagnetic XY phase breaks the $U(1)$ symmetry and contributes to the strong gapless mode at (π, π) . The spectrum weight is concentrated in the V-shaped structure around (π, π) , and the gap at $(0, 0)$ is proportional to the magnetic field as shown in Figs. 7(a)-(d). In the fully polarized phase, all spins are polarized, and the excitation with apparent dispersion structure mainly consists

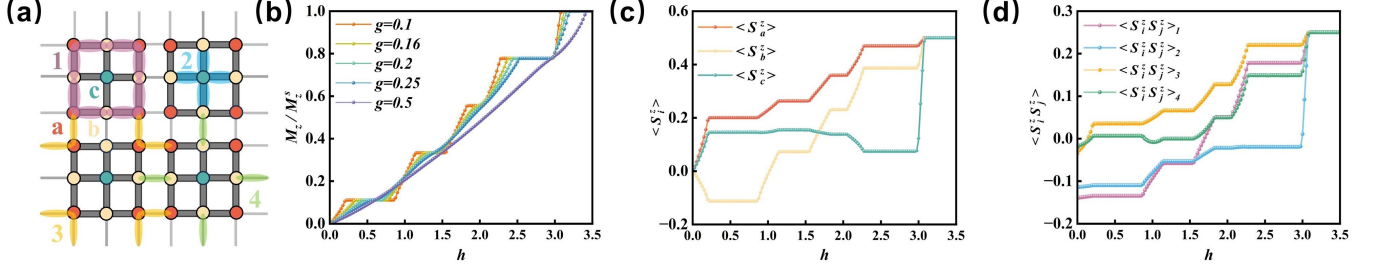


FIG. 5. (a) The structure of the 3×3 checkerboard lattice, where we use the same color to represent the equivalent spins and spin correlations. (b) The ratio of magnetization and saturated magnetization versus the magnetic field. (c) The magnetization of spins a, b, and c with $g=0.1$ versus the magnetic field. (d) The spin correlations $\langle S_i^z S_j^z \rangle_1$, $\langle S_i^z S_j^z \rangle_2$, $\langle S_i^z S_j^z \rangle_3$, and $\langle S_i^z S_j^z \rangle_4$ with $g=0.1$ versus the magnetic field.

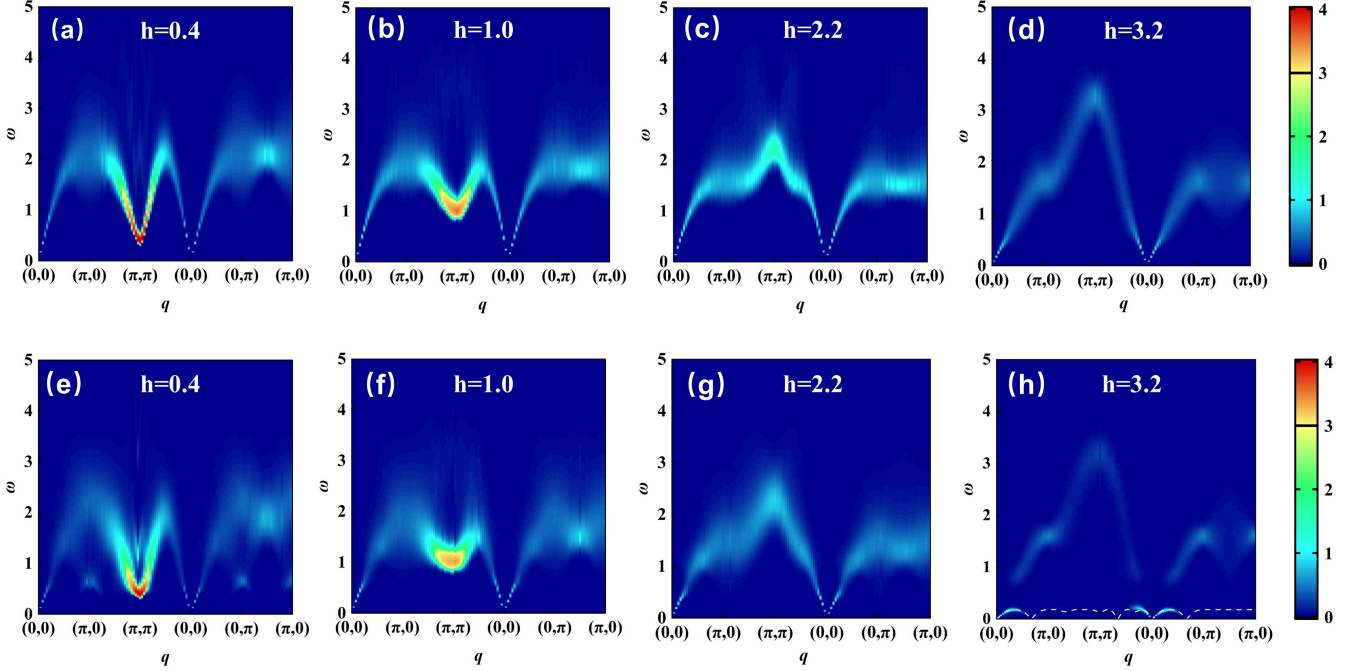


FIG. 6. Dynamic spin structure factor $S^{zz}(q, \omega)$ of 3×3 checkerboard model obtained from QMC-SAC calculations in a fixed coupling ratio $g=0.7$ (a)-(d) and $g=0.4$ (e)-(h) with different h . Panels (a)-(h) are in the non-plateau XY phase. To present the results of SAC more clearly, we take the value $U_0=3$ corresponding to the black bar as the boundary. Below the boundary, the spectral function is linearly mapped to the color bar, while above the boundary, it is a logarithmic mapping, $U = U_0 + \log_{10} S(q, \omega) - \log_{10} U_0$.

of the magnons as shown in Fig. 7(e).

When $g=0.4$, for the spectra of $S^{zz}(q, \omega)$, the low-energy branch along the path from $(0,0) \rightarrow (\pi, 0) \rightarrow (\pi, \pi)$ in the weak magnetic field as shown in Fig. 6(e), due to the Brillouin zone folding. As the magnetic field increases, the gap at (π, π) increases, and the branch with the folding feature merges with high-energy parts and then forms a single magnon excitation mode. In Figs 6(g)-(h), the spontaneous decay of magnons is intenser than in the case of $g=0.7$. As g decreases, the increase in magnetization under the same magnetic field as shown in Fig. 3, leading to a decrease in the weight of the spectrum. Notably, we observe the distinct separation of

the gapped high-energy part and gapless branch in the strong magnetic field as shown in Fig. 6(h). The high-energy part has energy around J_1 , which originates from intra-sublattice. The low-energy gapless branch exhibits periodic structure and energy around J_2 , with the gapless points at $(2\pi/3, 0)$ and $(2\pi/3, 2\pi/3)$, due to the folding of the Brillouin zone. To analyze low-energy magnon, we use spin waves of the effective Hamiltonian to fit the ω of each wave vector with the strongest weight extracted from the low-energy gapless branch, the spin wave is defined as [44, 45]

$$\omega_k = 4J_{eff} S_{eff} \sqrt{(1 - \gamma_k)(1 + \gamma_k \cos 2\theta)}, \quad (10)$$

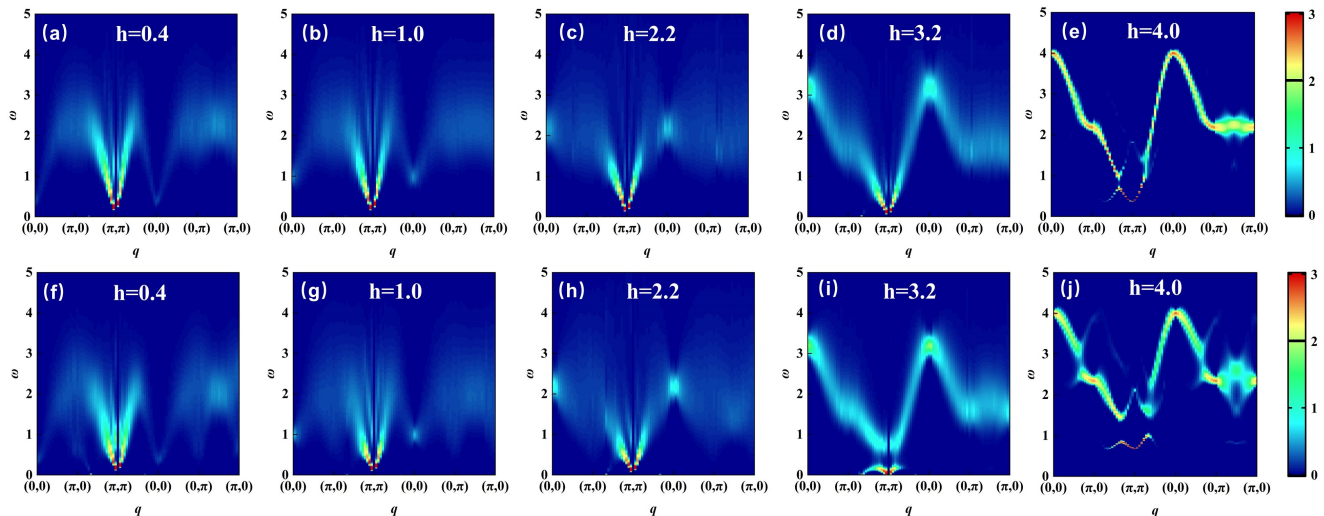


FIG. 7. Dynamic spin structure factor $S^\pm(q, \omega)$ of 3×3 checkerboard model obtained from QMC-SAC calculations in a fixed coupling ratio $g=0.7$ (a)-(e) and $g=0.4$ (f)-(j) with different h . Panels (a)-(d) and (f)-(i) are in the non-plateau XY phase, (e) and (g) are in the fully polarized phase. We take the value $U_0=2$ corresponding to the black bar as the boundary. Below the boundary, the spectral function is linearly mapped to the color bar, while above the boundary, it is a logarithmic mapping, $U = U_0 + \log_{10} S(q, \omega) - \log_{10} U_0$.

where J_{eff} is the effective interaction between 3×3 sublattice, S_{eff} is the effective spin number, $\gamma_k = (\cos 3k_x + \cos 3k_y)/2$ and $\sin \theta = h_{eff}/(8J_{eff}S_{eff})$. We find that the dotted line represents the result of the spin waves of effective Hamiltonian fits the gapless branch well. More details of fitting results can be found in Fig. 8. In the spectra of $S^\pm(q, \omega)$, Fig. 7(f) show the gapless point at $(\pi, \pi/3)$ and $(\pi/3, \pi/3)$, which originates from the Brillouin zone folding. We observe that the high-energy part with the gap separates from the gapless branch in the strong magnetic field. Fig. 7(i) shows the periodic structure, due to the Brillouin zone folding. Moreover, the gapless branch with obvious characteristics of antiferromagnetic XY phase comes from the excitation of inter-sublattice. In the fully polarized phase, energy gaps appear at the Brillouin zone folding points. Notably, the completely separated low-energy branch is a localized excitation similar to the excitation of the magnetization plateau phase, which we will discuss in detail later.

When $g=0.1$, we firstly focus on the spectra of $S^{zz}(q, \omega)$ and $S^\pm(q, \omega)$ in the non-plateau XY phase, the gapped high-energy and low-energy gapless branch are completely separated even in the weak magnetic field as shown in Fig. 9. The structure of the gapless branch is similar to Figs. 6(h) and 7(i). Notably, the values of $J_{eff}S_{eff}$ obtained via spin wave fitting are distinct in different magnetic fields as shown in Table II, which may be related to the magnetic order of the system. The spectral weight of $S^{zz}(q, \omega)$ and $S^\pm(q, \omega)$ are concentrated at the ω corresponding near the value of magnetic field at (π, π) and $(0,0)$, respectively. In Figs. 9 (a) and (e), the

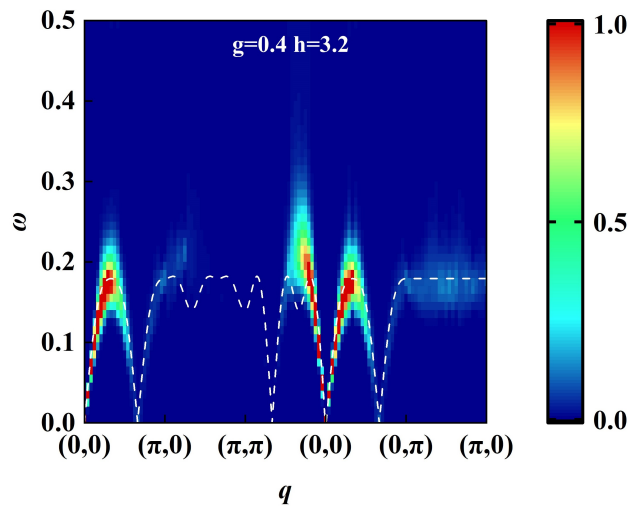


FIG. 8. Low-energy gapless branch of $g=0.4$ and $h=3.2$ extracted from Fig. 6(h). The dashed line is the result of fitting the ω corresponding to the strongest weight of each wave vector from the low-energy gapless branch with the spin wave of the effective Hamiltonian. The high decay of magnons causes the weight of the spectrum near (π, π) tend to vanish in the strong magnetic field.

spectral weight is concentrated at the low-energy branch, while for other cases is at the high-energy part. At the high-energy regime, the continuum is observed, which is dominated by the excitation of intra-sublattice.

In the magnetization plateau phase and fully polarized phase, we take h as 0.5, 1.45, 1.95, and 2.8 respectively

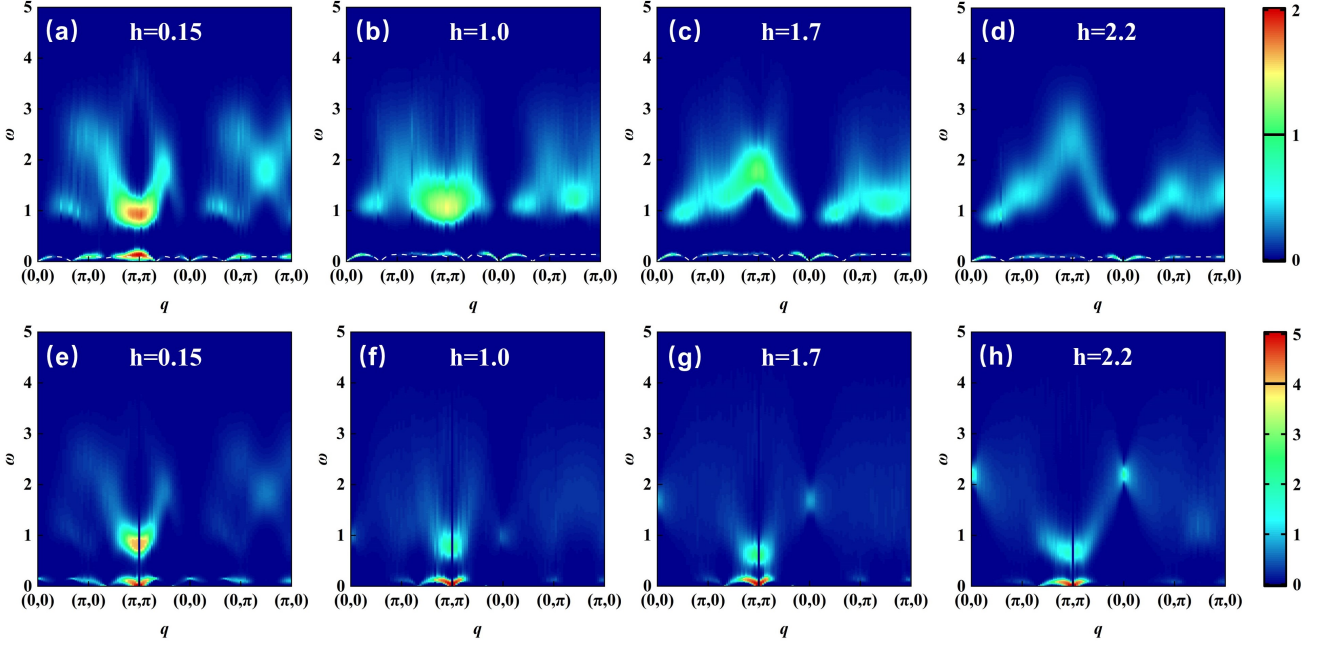


FIG. 9. Dynamic spin structure factor $S^{zz}(q, \omega)$ (a)-(d) and $S^{\pm}(q, \omega)$ (e)-(h) of 3×3 checkerboard model obtained from QMC-SAC calculations in a fixed coupling ratio $g=0.1$ with different h . Panels (a)-(h) are in the non-plateau XY phase. The dashed lines represent the results of spin wave fitting. We take the values of U_0 equal to 1 and 4 for $S^{zz}(q, \omega)$ and $S^{\pm}(q, \omega)$ respectively, corresponding to the black bar as the boundary. Below the boundary, the spectral function is linearly mapped to the color bar, while above the boundary, it is a logarithmic mapping, $U = U_0 + \log_{10}S(q, \omega) - \log_{10}U_0$.

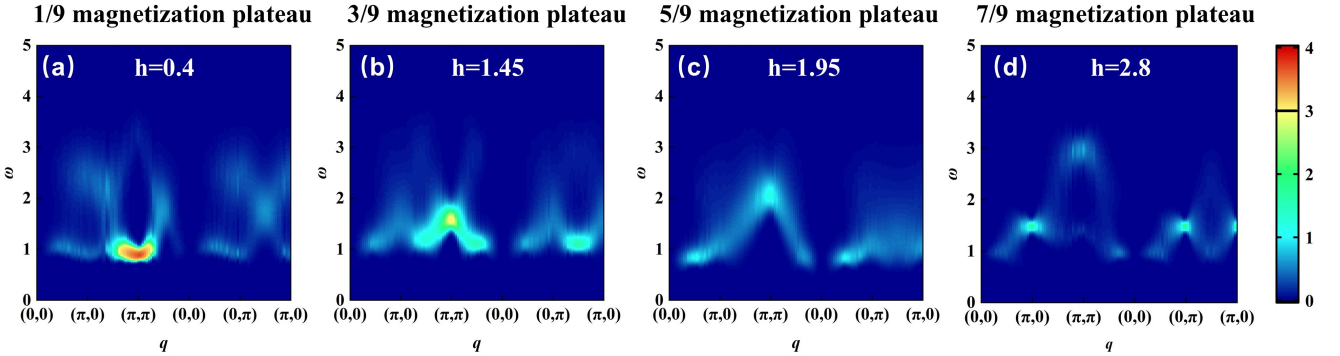


FIG. 10. Dynamic spin structure factor $S^{zz}(q, \omega)$ of 3×3 checkerboard model obtained from QMC-SAC calculations in a fixed coupling ratio $g=0.1$ in the different magnetization plateau phases. We take the value $U_0=3$ corresponding to the black bar as the boundary. Below the boundary, the spectral function is linearly mapped to the color bar, while above the boundary, it is a logarithmic mapping, $U = U_0 + \log_{10}S(q, \omega) - \log_{10}U_0$.

corresponding to $1/9$, $3/9$, $5/9$, and $7/9$ magnetization plateau to study the dynamic properties $S^{zz}(q, \omega)$ and $S^{\pm}(q, \omega)$ as shown in Figs. 10 and 11. We observe that the low-energy gapless excitations vanish, and the excitations are gapped in the all momentum space as expected and have energy around J_1 in the magnetization plateau phase, which is dominated by the localized excitation from the intra-sublattice. For the $S^{zz}(q, \omega)$, the spectrum structures in respective magnetization plateaus

are invariant for the same g . Notably, for the $S^{\pm}(q, \omega)$, we find the lower spectrum of low-energy excitations with $\Delta m=-1$ transition to the high-energy regime, while the high-energy excitations with $\Delta m=1$ transition to the low-energy regime. The weight of the spectrum is concentrated at the low-energy branches near (π, π) . It should be noted that these excitations are internal excitations of 3×3 sublattice propagating in momentum space. To explain the excitation mechanism of the energy branches

TABLE II. When $g=0.1$, the values of $J_{eff}S_{eff}$ are obtained by fitting the ω corresponding to the strongest weight of each wave vector from the low-energy gapless branch in different magnetic fields with the spin wave of the effective Hamiltonian.

Magnetic field h	$J_{eff}S_{eff}$
0.15	0.0239
1.0	0.0346
1.7	0.035
2.2	0.0235
3.04	0.0054

that transition with the magnetic field, we adopt the perturbation theory, which are discussed in detail later. The results of perturbation theory are agree well with QMC-SAC as shown in Fig. 11(a)-(e). In the fully polarized phase $h=4.0$, the energy gap of the Brillouin zone folding point increases, and the high-energy magnon exhibits a periodic structure. The flat bands originate from localized excitation, which matches the results of perturbation theory.

IV. DISCUSSION

When g is small, the system emerges the magnetization plateau phase as the magnetic field increases, and the J_2 can be considered as a perturbation of isolated 3×3 sublattice. To better understand the excitation in the magnetization plateaus, it is meaningful to analyze the excitation spectrum of the isolated 3×3 sublattice. We use exact diagonalization to analyze the excitation spectrum of isolated 3×3 sublattice in a longitudinal magnetic field. The magnetic field induces the energy level splitting, while the spin quantum numbers and magnetic quantum numbers remain invariant. In Fig 12, the ground state of the $1/9$, $3/9$, $5/9$ and $7/9$ magnetization plateaus are $S=1/2$ $m=1/2$, $S=3/2$ $m=3/2$, $S=5/2$ $m=5/2$ and $S=7/2$ $m=7/2$, respectively. For low-energy excited states, the energy levels with $\Delta m=-1$ transition to the high-energy part, while energy levels with $\Delta m=1$ transition to the low-energy regime and become the ground state of the next magnetization plateau until the system enters the fully polarized phase.

To investigate the excitation mechanism of the 3×3 checkerboard model in small coupling J_2 , we adopt a perturbation analysis. In the magnetization plateau phase and fully polarized phase, the magnetic quantum numbers of each 3×3 sublattice are $1/2$, $3/2$, $5/2$, $7/2$, and $9/2$ corresponding the $1/9$, $3/9$, $5/9$, $7/9$ magnetization plateaus and fully polarized phase. Therefore, we can construct the wave function of this model by multiplying the ground state of each isolated 3×3 sublattice

$$|\psi_g\rangle = |0\rangle_1 \otimes |0\rangle_2 \cdots |0\rangle_r \cdots |0\rangle_N, \quad (11)$$

where $|0\rangle$ is the ground state of isolated 3×3 sublattice. If the r -th sublattice is excited from ground state $|0\rangle$ to $|n\rangle$ excited state, the wave function of the model is

$$|\psi_e\rangle = |0\rangle_1 \otimes |0\rangle_2 \cdots |n\rangle_r \cdots |0\rangle_N, \quad (12)$$

the excited state in momentum space can be obtained through the Fourier transform

$$|\psi^q\rangle = \frac{1}{\sqrt{N}} \sum_{r=1}^N e^{-iqr} |\psi\rangle_r. \quad (13)$$

Thus, the dispersion relations in the reduced Brillouin zone can be obtained as

$$\epsilon(q) = \langle \psi_e^q | H | \psi_e^q \rangle - \langle \psi_g^q | H | \psi_g^q \rangle. \quad (14)$$

According to the Hamiltonian, we find that the result of dispersion relations are mainly dependent on the excited 3×3 sublattice and their neighbors. For the low-energy part of the transverse excitation spectra as shown in Fig. 11, the dispersion relations of low-energy excitation from $|0\rangle$ to $|n\rangle$ with $|\Delta m|=1$ can well describe the QMC results of the low-energy excitation with strong spectral weight no matter how large the magnetic field is. However, due to the results of QMC-SAC showing the continuum in the high-energy region in the magnetization plateau phase, it is challenging to distinguish the corresponding dispersions.

V. CONCLUSION

In this paper, we use the SSE-QMC to investigate the phase diagram of the $S=1/2$ Heisenberg model with a 3×3 checkerboard structure in a longitudinal magnetic field. The phase diagram presents the non-plateau XY phase, $1/9$, $3/9$, $5/9$, and $7/9$ magnetization plateau phases, and the fully polarized phase. We obtain the precise phase transition critical point via finite-size scalings and verify that the phase transition belongs to the 3D XY universality class. The model exhibits $1/9$, $3/9$, $5/9$, and $7/9$ magnetization plateaus with magnetic field for small g . The width of the magnetization plateaus will decrease until it completely vanishes under the competition of interaction and magnetic field as the g increases. Notably, the magnetizations and spin correlations remain invariant in the magnetization plateau phase.

Furthermore, the longitudinal and transverse dynamic structural factors exhibit different properties in a longitudinal magnetic field. In the non-plateau XY phase, gapless Goldstone modes are observed at $(0,0)$ for $S^{zz}(q, \omega)$ and (π, π) for $S^\pm(q, \omega)$. When g is large enough, the structures of the spectrum are similar to the square lattice in a magnetic field. As g decreases, the intense magnetic field causes the continuum to split into low-energy gapless branches and high-energy parts, where the low-energy gapless branches with periodic structure can be

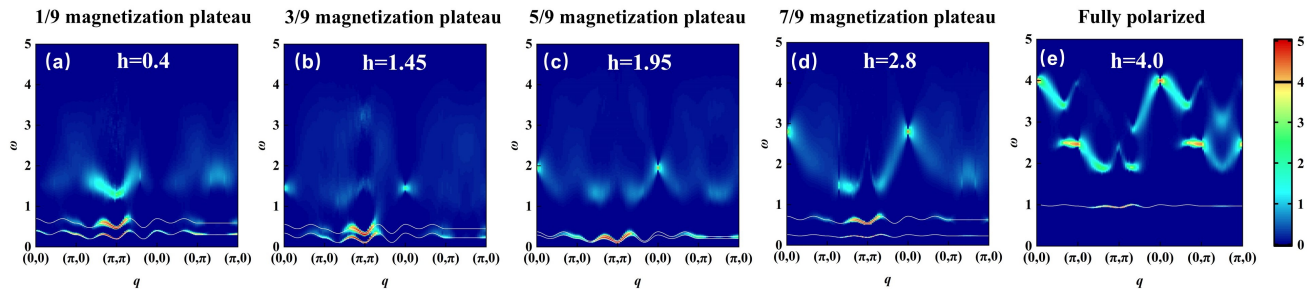


FIG. 11. Dynamic spin structure factor $S^\pm(q, \omega)$ of 3×3 checkerboard model obtained from QMC-SAC calculations in a fixed coupling ratio $g=0.1$ in different magnetization plateau phase. The white solid lines represent the dispersion relations of $|\Delta m|=1$. We take the value $U_0=4$ corresponding to the black bar as the boundary. Below the boundary, the spectral function is linearly mapped to the color bar, while above the boundary, it is a logarithmic mapping, $U = U_0 + \log_{10} S(q, \omega) - \log_{10} U_0$.

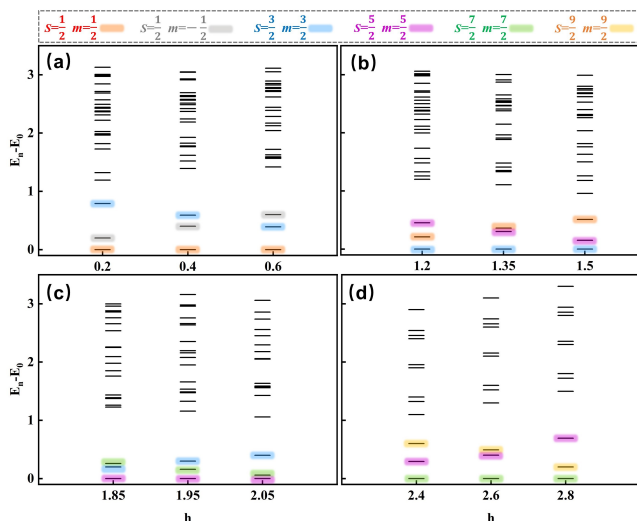


FIG. 12. Energy levels with $|\Delta m| = 1$ of 3×3 isolated plaquette in different phases, where (a) 1/9 magnetization plateau phase, (b) 3/9 magnetization plateau phase, (c) 5/9 magnetization plateau phase and (d) 7/9 magnetization plateau phase.

described by the spin wave in the canted antiferromag-

netic phase of effectively Hamiltonian. In the magnetization plateau phase, the excitations are gapped and localized, where the perturbation theory captures the low-energy localized excitations well in the transverse spectra. In the fully polarized phase, the spectra are composed of magnon and localized high-energy excitations for small g . Notably, previous works have successfully developed a viable method for implementing the expected checkerboard model in the optical lattice through cold atom experiments [46–50]. This work helps us better understand the properties of quantum magnetic materials with the structure of this model in a longitudinal magnetic field and provides a theoretical basis for checkerboard models with more odd spins sublattice in a longitudinal magnetic field.

ACKNOWLEDGMENTS

We thank Anders W. Sandvik, Han-Qing Wu, Jun-Qing Cheng, Zenan Liu, and Muwei Wu for helpful discussions. This project is supported by NKRDP-2022YFA1402802, NSFC-92165204, Leading Talent Program of Guangdong Special Projects (201626003), Guangdong Provincial Key Laboratory of Magnetoelectric Physics and Devices (No. 2022B1212010008), and Shenzhen Institute for Quantum Science and Engineering (No. SIQSE202102).

-
- [1] E. Manousakis, The spin- $\frac{1}{2}$ Heisenberg antiferromagnet on a square lattice and its application to the cuprous oxides, *Rev. Mod. Phys.* **63**, 1 (1991).
 - [2] V. Barzykin and D. Pines, Magnetic scaling in cuprate superconductors, *Phys. Rev. B* **52**, 13585 (1995).
 - [3] P. A. Lee, N. Nagaosa, and X.-G. Wen, Doping a mott insulator: Physics of high-temperature superconductivity, *Rev. Mod. Phys.* **78**, 17 (2006).
 - [4] B. M. Andersen, P. J. Hirschfeld, A. P. Kampf, and M. Schmid, Disorder-induced static antiferromagnetism in cuprate superconductors, *Phys. Rev. Lett.* **99**, 147002 (2007).
 - [5] D. Hu, X. Lu, W. Zhang, H. Luo, S. Li, P. Wang, G. Chen, F. Han, S. R. Banjara, A. Sapkota, A. Kreyssig, A. I. Goldman, Z. Yamani, C. Niedermayer, M. Skoulatos, R. Georgii, T. Keller, P. Wang, W. Yu, and P. Dai, Structural and magnetic phase transitions near optimal superconductivity in $\text{BaFe}_2(\text{As}_{1-x}\text{P}_x)_2$, *Phys. Rev. Lett.* **114**, 157002 (2015).
 - [6] T. Jungwirth, X. Marti, P. Wadley, and J. Wunderlich, Antiferromagnetic spintronics, *Nat. Nanotechnol.* **11**, 231 (2016).
 - [7] F. Haldane, Continuum dynamics of the 1-D Heisenberg antiferromagnet: Identification with the $O(3)$ nonlinear

- sigma model, *Phys. Lett. A* **93**, 464 (1983).
- [8] F. D. M. Haldane, Nonlinear field theory of large-spin heisenberg antiferromagnets: Semiclassically quantized solitons of the one-dimensional easy-axis néel state, *Phys. Rev. Lett.* **50**, 1153 (1983).
- [9] M. Oshikawa, M. Yamanaka, and I. Affleck, Magnetization Plateaus in Spin Chains: “Haldane Gap” for Half-Integer Spins, *Phys. Rev. Lett.* **78**, 1984 (1997).
- [10] M. Ye and A. V. Chubukov, Half-magnetization plateau in a heisenberg antiferromagnet on a triangular lattice, *Phys. Rev. B* **96**, 140406 (2017).
- [11] T. Susuki, N. Kurita, T. Tanaka, H. Nojiri, A. Matsuo, K. Kindo, and H. Tanaka, Magnetization Process and Collective Excitations in the $S=1/2$ Triangular-Lattice Heisenberg Antiferromagnet $\text{Ba}_3\text{CoSb}_2\text{O}_9$, *Phys. Rev. Lett.* **110**, 267201 (2013).
- [12] Y. Shirata, H. Tanaka, A. Matsuo, and K. Kindo, Experimental Realization of a Spin-1/2 Triangular-Lattice Heisenberg Antiferromagnet, *Phys. Rev. Lett.* **108**, 057205 (2012).
- [13] T. Ono, H. Tanaka, H. Aruga Katori, F. Ishikawa, H. Mitamura, and T. Goto, Magnetization plateau in the frustrated quantum spin system Cs_2CuBr_4 , *Phys. Rev. B* **67**, 104431 (2003).
- [14] M. E. Zhitomirsky, A. Honecker, and O. A. Petrenko, Field induced ordering in highly frustrated antiferromagnets, *Phys. Rev. Lett.* **85**, 3269 (2000).
- [15] K. Morita and N. Shibata, Field-Induced Quantum Phase Transitions in $S = 1/2$ J_1 - J_2 Heisenberg Model on Square Lattice, *J. Phys. Soc. Jpn.* **85**, 094708 (2016).
- [16] T. Coletta, M. E. Zhitomirsky, and F. Mila, Quantum stabilization of classically unstable plateau structures, *Phys. Rev. B* **87**, 060407 (2013).
- [17] P. Thalmeier, M. E. Zhitomirsky, B. Schmidt, and N. Shannon, Quantum effects in magnetization of J_1 - J_2 square lattice antiferromagnet, *Phys. Rev. B* **77**, 104441 (2008).
- [18] K. Morita and N. Shibata, Multiple magnetization plateaus and magnetic structures in the $S = \frac{1}{2}$ Heisenberg model on the checkerboard lattice, *Phys. Rev. B* **94**, 140404 (2016).
- [19] S. Capponi, Numerical study of magnetization plateaus in the spin- $\frac{1}{2}$ heisenberg antiferromagnet on the checkerboard lattice, *Phys. Rev. B* **95**, 014420 (2017).
- [20] R. Coldea, S. M. Hayden, G. Aeppli, T. G. Perring, C. D. Frost, T. E. Mason, S.-W. Cheong, and Z. Fisk, Spin Waves and Electronic Interactions in La_2CuO_4 , *Phys. Rev. Lett.* **86**, 5377 (2001).
- [21] N. S. Headings, S. M. Hayden, R. Coldea, and T. G. Perring, Anomalous High-Energy Spin Excitations in the High- T_c Superconductor-Parent Antiferromagnet La_2CuO_4 , *Phys. Rev. Lett.* **105**, 247001 (2010).
- [22] T. Masuda, S. Kitaoka, S. Takamizawa, N. Metoki, K. Kaneko, K. C. Rule, K. Kiefer, H. Manaka, and H. Nojiri, Instability of magnons in two-dimensional antiferromagnets at high magnetic fields, *Phys. Rev. B* **81**, 100402 (2010).
- [23] G.-Y. Sun, Y.-C. Wang, C. Fang, Y. Qi, M. Cheng, and Z. Y. Meng, Dynamical signature of symmetry fractionalization in frustrated magnets, *Phys. Rev. Lett.* **121**, 077201 (2018).
- [24] N. Ma, G.-Y. Sun, Y.-Z. You, C. Xu, A. Vishwanath, A. W. Sandvik, and Z. Y. Meng, Dynamical signature of fractionalization at a deconfined quantum critical point, *Phys. Rev. B* **98**, 174421 (2018).
- [25] J. E. Hoffman, E. W. Hudson, K. M. Lang, V. Madhavan, H. Eisaki, S. Uchida, and J. C. Davis, A four unit cell periodic pattern of quasi-particle states surrounding vortex cores in $\text{Bi}_2\text{Sr}_2\text{CaCu}_2\text{O}_{8+\delta}$, *Sci.* **295**, 466 (2002).
- [26] T. Hanaguri, C. Lupien, Y. Kohsaka, D.-H. Lee, M. Azuma, M. Takano, H. Takagi, and J. C. Davis, A ‘checkerboard’ electronic crystal state in lightly hole-doped $\text{Ca}_{2-x}\text{Na}_x\text{CuO}_2\text{Cl}_2$, *Nat.* **430**, 1001 (2004).
- [27] X. Ran, N. Ma, and D.-X. Yao, Criticality and scaling corrections for two-dimensional heisenberg models in plaquette patterns with strong and weak couplings, *Phys. Rev. B* **99**, 174434 (2019).
- [28] Y. Xu, Z. Xiong, H.-Q. Wu, and D.-X. Yao, Spin excitation spectra of the two-dimensional $S = \frac{1}{2}$ Heisenberg model with a checkerboard structure, *Phys. Rev. B* **99**, 085112 (2019).
- [29] J.-Q. Cheng, J. Li, Z. Xiong, H.-Q. Wu, A. W. Sandvik, and D.-X. Yao, Fractional and composite excitations of antiferromagnetic quantum spin trimer chains, *npj Quantum Mater.* **7**, 3 (2022).
- [30] A. K. Bera, S. Yusuf, S. K. Saha, M. Kumar, D. Voneshen, Y. Skourski, and S. A. Zvyagin, Emergent many-body composite excitations of interacting spin-1/2 trimers, *Nat. Commun.* **13**, 6888 (2022).
- [31] Y. Shen, J. Sears, G. Fabbris, A. Weichselbaum, W. Yin, H. Zhao, D. G. Mazzone, H. Miao, M. H. Upton, D. Casa, R. Acevedo-Esteves, C. Nelson, A. M. Barbour, C. Mazzoli, G. Cao, and M. P. M. Dean, Emergence of Spinons in Layered Trimer Iridate $\text{Ba}_4\text{Ir}_3\text{O}_{10}$, *Phys. Rev. Lett.* **129**, 207201 (2022).
- [32] G. Cao, H. Zheng, H. Zhao, Y. Ni, C. A. Pocs, Y. Zhang, F. Ye, C. Hoffmann, X. Wang, M. Lee, et al., Quantum liquid from strange frustration in the trimer magnet $\text{Ba}_4\text{Ir}_3\text{O}_{10}$, *npj Quantum Mater.* **5**, 26 (2020).
- [33] X. Chen, Y. He, S. Wu, Y. Song, D. Yuan, E. Bourret-Courchesne, J. P. C. Ruff, Z. Islam, A. Frano, and R. J. Birgeneau, Structural and magnetic transitions in the planar antiferromagnet $\text{Ba}_4\text{Ir}_3\text{O}_{10}$, *Phys. Rev. B* **103**, 224420 (2021).
- [34] A. Sokolik, S. Hakani, S. Roy, N. Pellatz, H. Zhao, G. Cao, I. Kimchi, and D. Reznik, Spinons and damped phonons in the spin- $\frac{1}{2}$ quantum liquid $\text{Ba}_4\text{Ir}_3\text{O}_{10}$ observed by Raman scattering, *Phys. Rev. B* **106**, 075108 (2022).
- [35] M. Majumder, S. Kanungo, A. Ghoshray, M. Ghosh, and K. Ghoshray, Magnetism of the spin-trimer compound $\text{CaNi}_3(\text{P}_2\text{O}_7)_2$: Microscopic insight from combined ^{31}P NMR and first-principles studies, *Phys. Rev. B* **91**, 104422 (2015).
- [36] Y.-Y. Chang, J.-Q. Cheng, H. Shao, D.-X. Yao, and H.-Q. Wu, Magnon, doublon and quarton excitations in 2D $S=1/2$ trimerized Heisenberg models, *Front. Phys.* **19**, 1 (2024).
- [37] J.-Q. Cheng, Z.-Y. Ning, H.-Q. Wu, and D.-X. Yao, Quantum phase transitions and composite excitations of antiferromagnetic quantum spin trimer chains in a magnetic field, [arXiv:2402.00272](https://arxiv.org/abs/2402.00272) (2024).
- [38] O. F. Syljuåsen and A. W. Sandvik, Quantum monte carlo with directed loops, *Phys. Rev. E* **66**, 046701 (2002).
- [39] H. Shao, Y. Q. Qin, S. Capponi, S. Chesi, Z. Y. Meng, and A. W. Sandvik, Nearly deconfined spinon excitations in the square-lattice spin-1/2 heisenberg antiferromag-

- net, *Phys. Rev. X* **7**, 041072 (2017).
- [40] H. Shao and A. W. Sandvik, Progress on stochastic analytic continuation of quantum monte carlo data, *Physics Reports* **1003**, 1 (2023), progress on stochastic analytic continuation of quantum Monte Carlo data.
- [41] M. P. A. Fisher, P. B. Weichman, G. Grinstein, and D. S. Fisher, Boson localization and the superfluid-insulator transition, *Phys. Rev. B* **40**, 546 (1989).
- [42] M. Campostrini, M. Hasenbusch, A. Pelissetto, P. Rossi, and E. Vicari, Critical behavior of the three-dimensional XY universality class, *Phys. Rev. B* **63**, 214503 (2001).
- [43] A. Lüscher and A. M. Läuchli, Exact diagonalization study of the antiferromagnetic spin- $\frac{1}{2}$ heisenberg model on the square lattice in a magnetic field, *Phys. Rev. B* **79**, 195102 (2009).
- [44] O. F. Syljuåsen, Numerical evidence for unstable magnons at high fields in the heisenberg antiferromagnet on the square lattice, *Phys. Rev. B* **78**, 180413 (2008).
- [45] S. Shinkevich, O. F. Syljuåsen, and S. Eggert, Spin-wave calculation of the field-dependent magnetization pattern around an impurity in heisenberg antiferromagnets, *Phys. Rev. B* **83**, 054423 (2011).
- [46] K. Góral, L. Santos, and M. Lewenstein, Quantum phases of dipolar bosons in optical lattices, *Phys. Rev. Lett.* **88**, 170406 (2002).
- [47] M. Ölschläger, G. Wirth, T. Kock, and A. Hemmerich, Topologically induced avoided band crossing in an optical checkerboard lattice, *Phys. Rev. Lett.* **108**, 075302 (2012).
- [48] G. Wirth, M. Ölschläger, and A. Hemmerich, Evidence for orbital superfluidity in the p-band of a bipartite optical square lattice, *Nat. Phys.* **7**, 147 (2011).
- [49] X. Wu, X. Liang, Y. Tian, F. Yang, C. Chen, Y.-C. Liu, M. K. Tey, and L. You, A concise review of rydberg atom based quantum computation and quantum simulation*, *Chin. Phys. B* **30**, 020305 (2021).
- [50] G. Semeghini and H. Levine and A. Keesling and S. Ebadi and T. T. Wang and D. Bluvstein and R. Verresen and H. Pichler and M. Kalinowski and R. Samajdar and A. Omran and S. Sachdev and A. Vishwanath and M. Greiner and V. Vuletić and M. D. Lukin , Probing topological spin liquids on a programmable quantum simulator, *Sci.* **374**, 1242 (2021).